

Perovskite/silicon tandem solar cells: Effect of luminescent coupling and bifaciality

Klaus Jäger,^{*†} Peter Tillmann,^{*†} Eugene A. Katz,[‡] and Christiane Becker^{*}

June 9, 2022

The power conversion efficiency of the market-dominating silicon photovoltaics approaches its theoretical limit. Bifacial solar operation with harvesting additional light impinging on the module back and the perovskite/silicon tandem device architecture are among the most promising approaches for further increasing the energy yield from a limited area. Here, we calculate the energy output of perovskite/silicon tandem solar cells in monofacial and bifacial operation considering, for the first time, luminescent coupling between two sub-cells. For energy yield calculations we study idealized solar cells at both, standard testing as well as realistic weather conditions in combination with a detailed illumination model for periodic solar panel arrays. Considering typical, experimental photoluminescent quantum yield values we find that more than 50% of excess electron-hole pairs in the perovskite top cell can be utilized by the silicon bottom cell by means of luminescent coupling. As a result, luminescent coupling strongly relaxes the constraints on the top-cell bandgap in monolithic tandem devices. In combination with bifacial operation, the optimum perovskite bandgap shifts from 1.71 eV to the range 1.60-1.65 eV where already high-quality perovskite materials exist. The results can hence change a paradigm in developing the optimum perovskite material for tandem solar cells.

^{*}Helmholtz-Zentrum Berlin für Materialien und Energie, Albert-Einstein-Straße 16, D-12489 Berlin.

[†]Zuse Institute Berlin, Takustraße 7, D-14195 Berlin.

[‡]Dept. of Solar Energy and Environmental Physics, The Jacob Blaustein Institutes for Desert Research, Ben-Gurion University of the Negev, Sede Boqer Campus, 8499000 Israel.

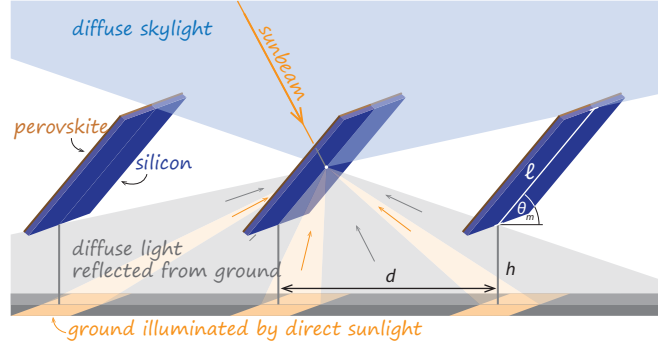


Figure 1: Illustrating the illumination components reaching a bifacial solar module in a large photovoltaic field: both, the front and back sides, can be illuminated by direct sunlight, diffuse skylight, and light from the ground, which can originate from direct sunlight or diffuse skylight. The photovoltaics field is characterized by the module length ℓ , height of the modules above the ground h , module tilt angle θ_m , distance between rows of modules d and albedo of the ground A .⁶

1. Introduction

Monofacial silicon solar cells currently dominate the photovoltaic (PV) market.¹ Their practical efficiencies meanwhile approach the theoretical limit of around 29.4%,² such that innovative technologies and concepts are required to increase the energy yield on limited areas. One approach is using bifacial solar systems that cannot only utilize light, which falls onto the front side of the PV module, but also light reaching the back side,^{3,4} as illustrated in Fig. 1. Bifacial photovoltaic power plants demonstrated $> 20\%$ enhanced annual energy yield in comparison to a monofacial power plant of a similar size.⁵ Modern silicon solar cell concepts with passivated emitter rear contact (PERx), heterojunction (SHJ) or integrated back contact (IBC) enable bifacial solar cell operation at low additional cost. Due to these reasons the International Technology Roadmap for Photovoltaics predicts nearly 70% market share for bifacial solar cells in 2030.¹

A second method to increase the energy output from a photovoltaic system on limited area is the multi-junction approach where multiple solar cells with different band gaps are stacked on top of each other. These different materials exhibit complementary electronic bandgaps such that the high energy photons of solar irradiation are absorbed by the high-bandgap materials on top, while the lower energy photons are absorbed by the lower bandgap material at the bottom. As a result the excess photon energy losses are reduced and conversion efficiencies increase, significantly overcoming the efficiency limit of silicon single-junction solar cells.

A currently widely investigated technology for large scale applications is the combination of silicon and perovskite solar cells in a tandem device.⁷ High efficiencies, a tunable bandgap, external photoluminescent quantum yields up to 10%⁸ and low-cost fabrication processes make perovskites an attractive tandem partner for established silicon photovoltaics. The current record efficiencies for perovskite/silicon tandem solar cells are 29.15%⁹ for monolithic two-terminal (2T) and 28.2%¹⁰ for stacked four-terminal (4T) devices, respectively, bearing the potential for power conversion efficiencies as high as $\approx 44\%$ ¹¹ assuming radiative recombination the only recombination channel and standard test conditions (STC), i.e. 25°C temperature and 1000 W/m² solar irradiance with AM1.5g spectral distribution.¹² The monolithic tandem configuration has (among others) the advantage of requiring only two external contacts and one maximum power point tracker, enabling module related costs comparable to single-junction devices.¹³ Under STC, the theoretical power output of silicon-based monolithic tandem solar cells, however, reveals a sharp maximum at a top-cell bandgap around 1.71 eV limiting the choice of available perovskite top cell materials. The reason for the sharp optimum is the current matching requirement in a monolithic series-connected tandem device, i.e. the top cell bandgap has to be tuned such that the same number of photons is absorbed in the top cell and the bottom cell. However, perovskites with band gaps above 1.7 eV often suffer from low electronic quality resulting in reduced solar-cell efficiencies.¹⁴

In recent years, bifacial perovskite/silicon tandem solar cells were extensively investigated.^{15–19} In particular, Onno *et al.* found that the range of appropriate top-cell bandgaps broadens in a bifacial tandem-cell configuration.¹⁶ This is in line with thermodynamic consideration by Khan *et al.*²⁰ Additional photons absorbed in the silicon bottom cell from rear side illumination allow for a lower bandgap of the (perovskite) top cell at current-matching conditions.

One aspect of perovskite-based tandem photovoltaic operation has not been considered so far: luminescent (or radiative) coupling between the different subcells in the device, i.e. the re-absorption of luminescent photons emitted by the high-bandgap top cell in the low-bandgap bottom cell. This effect is well-known in multi-junction solar cells based on III-V semiconductors. Already in 2002, Brown and Green identified luminescent coupling as a means to reduce spectral mismatch in two-terminal tandem solar cells.²¹ While the effect of luminescent coupling is negligible at current-matching conditions, a considerable positive effect appears in non-current-matched, bottom-cell limited devices.^{22–25} Similar to bifacial cell operation luminescent coupling, i.e. the re-absorption of luminescent photons emitted by the high-bandgap cell in the low-bandgap cell, results in more photons absorbed in the silicon bottom cell, as illustrated in Fig. 2. To the best of our knowledge, the potential relevance of luminescent coupling for perovskite-based tandem solar cells has not been addressed so far.

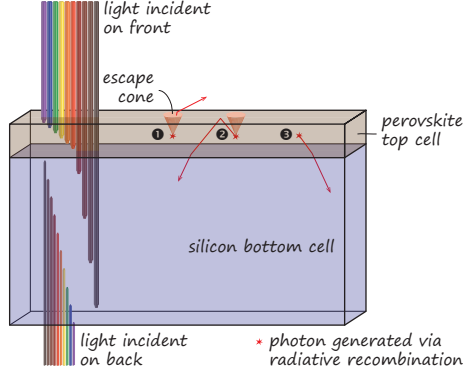


Figure 2: Illustrating luminescent coupling (LC) in a perovskite/silicon tandem solar cell. A photon, which is generated in the perovskite top cell via radiative recombination can (1) either leave the perovskite cell if its direction is within the escape cone, or (2) it undergoes total internal reflection and is redirected downward such that it can enter the silicon cell, just as (3) a photon that is emitted into the lower hemisphere. More details can be found in appendix C.

In this study, we theoretically investigate how bifacial illumination and luminescent coupling affect the performance of perovskite/silicon tandem solar cells. We use idealized solar-cell models for these calculations: Shockley-Queisser’s detailed balance limit²⁶ for the perovskite top cell and the Richter limit² for the silicon bottom cell, which also incorporates Auger recombination. For the perovskite cell operation under one Sun, Auger recombination is negligible.²⁷ Using these models, we first assess, how illumination from the back side and luminescent coupling affect the tandem-cell performance under standard test conditions. Then, we use optical simulations²⁸ to estimate, how much of light from radiative recombination in the perovskite leaves the cell towards the Sun in a single-junction cell configuration and how much will reach the silicon subcell in a tandem stack. This allows us to relate measured *external* quantum photoluminescence efficiency in a single-junction perovskite cell to the reasonable *internal* quantum efficiency, and subsequently to evaluate, which range of luminescent-coupling efficiencies is realistic in tandem devices. Last, we estimate the energy yield using weather data from a climatic zone with high diffuse illumination ratio. For this we apply a detailed illumination model, which takes direct sunlight, diffuse skylight, shadowing by other modules and reflection from the ground into account.⁶ We finally discuss how all the realistic deviations from standard test conditions considered in this study – (1) bifacial irradiation, (2) luminescent coupling and (3) weather conditions with high diffuse illumination ratio — influence the constraints for the perovskite top cell bandgap.

2. Modelling details

2.1. Electrical solar cell model

To calculate the current density-voltage (JV) characteristic of the PV modules, the irradiance values on the front and back sides are used as input for the electrical model. In this paper we use highly idealized solar cell models:

For the perovskite top cell we assume that all photons with energy higher than the cell band gap are absorbed and every absorbed photon generates one electron-hole pair. Hence, the maximum achievable photocurrent density is given by

$$J_{\text{ph, pero}} = e \int_0^{\lambda_{\text{pero}}} \Phi_f(\lambda) d\lambda, \quad (1)$$

where e is the elementary charge, Φ_f is the photon flux reaching the module at the front, and λ_{pero} is the wavelength corresponding to the perovskite bandgap. In a monolithic tandem device this value is only achieved in case of a limiting top cell, i.e. less or equal photons absorbed in the perovskite than in the silicon. The JV characteristic is calculated according to the *Shockley-Queisser* (SQ) limit,²⁶ where only radiative recombination is considered. In the SQ limit, both external (ELQE) and internal (ILQE) luminescence quantum efficiencies are equal to 100%. The former is the number of photons emitted into free space relative to the number of electron-hole pairs generated by light absorption in a solar cell. The latter is a ratio between the number of electron-hole pairs recombined radiatively to the entire number of the recombined pairs. The SQ limit is briefly summarized in appendix A.

For the silicon bottom cell, the perovskite top-cell acts as a filter for the short wavelengths up to the perovskite bandgap. However, the perovskite cell also may emit light, which can be utilized by the bottom cell via *luminescent coupling*, which is discussed below. Additionally, Auger recombination must be considered for a silicon cell. We implement this using an idealized model by Richter and coworkers;² the details are given in appendix B.

In a high-end solar cell made of a direct bandgap semiconductor a significant fraction of the absorbed photons, which are not extracted as electrical current, will be re-emitted as light via radiative recombination. An electrically independent solar cell operated at maximum power point only has a small recombination current because almost all charge carriers are extracted. However, in a two-terminal tandem cell, where the top and bottom cells are electrically connected in series, the same current density flows through bottom and top cell. If the generated photocurrent density and the extracted current density deviate strongly from each other, significant recombination will be present in the top cell. If the recombination is radiative, the re-emitted light from the

top cell can be absorbed and utilized by the bottom cell, which is known as *luminescent coupling* (LC). In perovskite/silicon tandem solar cells we only need to consider light emitted by the perovskite cell, which can be absorbed by the silicon bottom. The silicon cell itself will hardly emit light because of the indirect bandgap of silicon. Further, the energy of the emitted photons would be close to the silicon bandgap and hence cannot be absorbed by perovskite with a larger bandgap than silicon. For the maximum achievable short-circuit current density in the Si bottom cell we find

$$J_{\text{ph, Si}}(V_{\text{pero}}) = e \int_{\lambda_{\text{pero}}}^{\lambda_{\text{Si}}} A(\lambda) \Phi_f(\lambda) d\lambda + e \int_0^{\lambda_{\text{Si}}} A(\lambda) \Phi_b(\lambda) d\lambda + \eta_{\text{LC}} [J_{\text{ph, pero}} - J_{\text{pero}}(V_{\text{pero}})] \quad (2)$$

with the absorption in silicon $A(\lambda)$. We calculate the absorption in Si according to the Tiedje-Yablonovitch limit for a silicon wafer thickness of $300 \mu\text{m}$ as described in appendix B. $J_{\text{pero}}(V)$ is the current density at the working point of the perovskite cell. The term $[J_{\text{ph, pero}} - J_{\text{pero}}(V)]$ corresponds to excess electron-hole pairs generated in the perovskite top cell, which cannot be extracted from the monolithic tandem device, e.g. due to a limiting bottom cell. These excess electron-hole pairs can recombine radiatively and be re-absorbed by the silicon with η_{LC} being the efficiency of this luminescent coupling. Here we also accounted for light that hits the solar cell at the back, Φ_b . For monofacial cells we have $\Phi_b \equiv 0$. Further, λ_{Si} is the wavelength corresponding to the silicon bandgap. More details about luminescent coupling are given in appendix C.

Since we assume zero series resistance and infinitely large shunt resistance of the cells, for both subcells the electric current density J can be directly calculated from the photocurrent density J_{ph} and the voltage-dependent recombination current density J_{rec} ,

$$J = J_{\text{ph}} - J_{\text{rec}}(V), \quad (3)$$

where details about J_{rec} for the perovskite and silicon subcells are given in appendix A and appendix B, respectively.

For two-terminal cells, where the same current density flows through both cells, we have

$$J_{\text{cell}} = J_{\text{ph, Si}} - J_{\text{rec, Si}}(V_{\text{Si}}) = J_{\text{ph, pero}} - J_{\text{rec, pero}}(V_{\text{pero}}). \quad (4)$$

We calculate the JV characteristic of the tandem solar cell by numerically inverting $J_{\text{rec, Si}}(V_{\text{Si}})$ and $J_{\text{rec, pero}}(V_{\text{pero}})$ such that we have functions of $J_{\text{rec, pero}}$ and $J_{\text{rec, Si}}$, respectively. From the JV curve the output power density of the cell can be directly calculated as

$$P_{\text{cell}} = J_{\text{cell}} [V_{\text{Si}}(J_{\text{rec, Si}}) + V_{\text{pero}}(J_{\text{rec, pero}})], \quad (5)$$

$$P_{\text{mpp}} = \max_{J_{\text{cell}}} [P_{\text{cell}}].$$

Tandem solar cells can also be built in four-terminal configuration, where the two sub-cells are electrically independent and can operate at their individual maximum power points,

$$P_{\text{mpp}} = \max_{J_{\text{Si}}} [J_{\text{Si}} \cdot V_{\text{Si}}(J_{\text{rec,Si}})] + \max_{J_{\text{pero}}} [J_{\text{pero}} \cdot V_{\text{pero}}(J_{\text{rec,pero}})] . \quad (6)$$

2.2. Optical model

In order to estimate the effect of luminescent coupling in realistic perovskite-tandem solar cells, we apply optical modelling. In this paper, we use the MATLAB-based tool GenPro4, which can calculate the absorption profile in solar-cell structures using the net radiation method.²⁸ This tool treats light coherently in thin layers but incoherently in thick layers. Because GenPro4 only can treat light that falls onto a layer stack from the exterior, we split the simulations in two: one simulation treating the layer stack above the perovskite layer, the other layer stack treating the layers below. Details on these calculations are given in appendix D.

2.3. Energy yield calculation

We calculate the overall energy yield for different scenarios using a simulation approach that combines several sub models. For calculating the spectral irradiance at the front and back sides of a solar module in a big PV field, we employ a recently developed illumination model.^{6,29} The PV field is considered so large that boundary effects can be neglected. As schematically illustrated in Fig. 1, the illumination model considers four components reaching the module front: direct sunlight, diffuse skylight, diffuse light from the ground, which originates from direct sunlight reaching the ground and diffuse skylight reaching the ground. Further, the same four components must be considered reaching the back-side of the module. Hence the illumination model considers eight components in total.

The illumination model uses the following input parameters: first, the geometrical parameters of the PV field, which are sketched in Fig. 1: module length ℓ , mounting height h , module spacing d and tilt angle θ_m . Secondly, the albedo (i.e. the reflectivity) of the ground, which we assume to be independent of the wavelength for the moment. Thirdly, the (spectral) *direct normal incidence* (DNI) and the *diffuse horizontal incidence* (DHI) for different instants of time. We retrieve these data from the National Solar Radiation Data Base (NSRDB) operated by NREL.³⁰ They publish hourly spectral direct and diffuse irradiance for a *typical meteorological year* (TMY).

With the spectral irradiance on the front and back sides we can calculate the generated photocurrent densities in the top and bottom cells using eqn (1) and (2). We

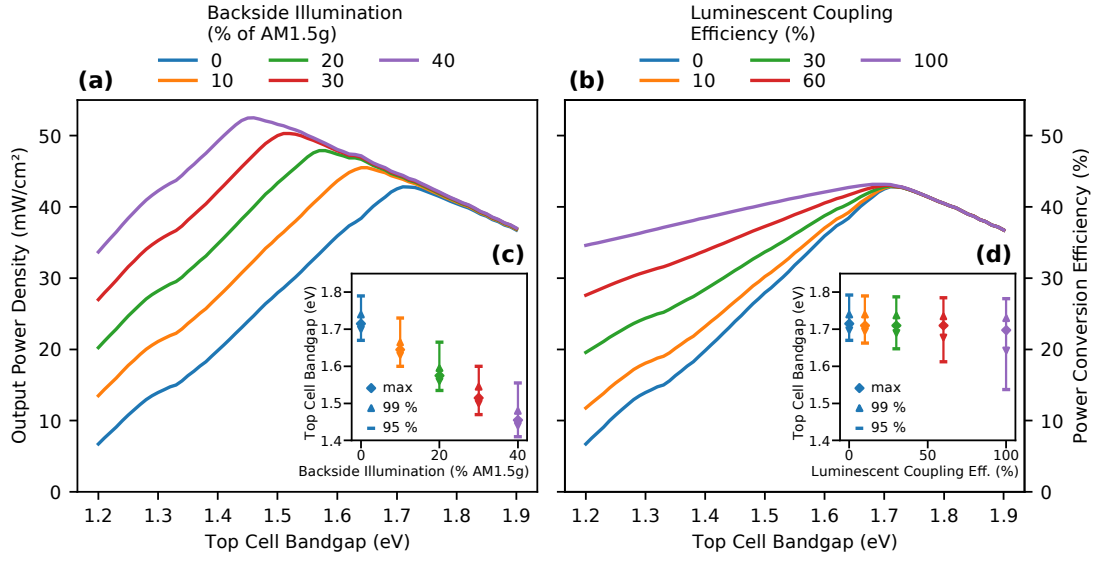


Figure 3: Maximum output power density of two-terminal tandem solar cells as function of the top-cell bandgap for different levels of (a) backside illumination and (b) luminescent coupling efficiencies under standard test conditions. The insets show the optimal top-cell bandgap for different levels of (c) backside illumination and (d) luminescent coupling efficiencies under standard test conditions. The diamonds mark the ideal bandgap with maximum power output; the arrowheads and the dash marks span the ranges where at least 99% and 95% of the maximum output power density are achieved. Note: For the graph with varying backside illumination no luminescent coupling is assumed and for varying luminescent coupling efficiencies no backside illumination is present. The bottom cell bandgap is 1.12 eV in all cases.

calculate the full JV -characteristics for every hour in the TMY data set and take the appropriate maximum to get the maximum power output of the cell according to eqn (20) and (21). By integrating over all hourly data points in the data set for one year we obtain the annual energy yield.

3. Results and discussion

3.1. Tandem-cell operation under standard testing conditions

Figure 3 shows the effect of the top cell bandgap on the maximum output power density of a two-terminal tandem solar cell for various levels of backside illumination (a)

and luminescent coupling (b) under standard testing conditions. Without either backside illumination or luminescent coupling the optimal bandgap of the perovskite cell for maximum power output density is 1.71 eV, where the same current densities are generated in the top and bottom cells. For other top-cell bandgaps, the generated current densities differ from each other. Only the lower current density can flow through the solar cell, while the *excess* current density is lost, which reduces the overall power conversion efficiency of the tandem solar cell. For a silicon-based tandem solar cell, the bandgap of the top cell absorber is critical to achieve current matching between the subcells. For a top-cell bandgap higher than the optimum, the current density generated in the top cell is below that generated in the bottom cell, the tandem cell is said to be “top-cell limited”. For a top-cell bandgap lower than the optimum, the bottom-cell current density is lower; the cell is “bottom-cell limited”.

With higher levels of backside illumination, as shown in Fig. 3(a), the maximum power output density increases and the optimum top-cell bandgap shifts towards lower bandgaps. The backside illumination is exclusively absorbed in the bottom cell and cannot reach the top cell, leading to more generated electron-hole pairs in the bottom-cell. To match the photocurrent densities between the two subcells, the top-cell bandgap needs to be lowered, such that it can absorb more light. For top-cell bandgaps larger than 1.71 eV, increased back-side illumination hardly affects the overall output power density, because here the tandem device is top-cell limited and the additional photocurrent generated in the bottom cell cannot be utilized.

As shown in Fig. 3(b), increasing the luminescent coupling efficiency does not shift the position and height of the maximum output power density; however, the power output is increased for bandgaps below the optimum. For top-cell bandgaps above the optimum, luminescent coupling does not affect the performance, because here the cells are top-cell limited and the excess current in the bottom cell cannot be utilized for luminescent coupling.

The insets in Fig. 3 summarize these results. For a given scenario of backside illumination or luminescent coupling the optimal bandgap and the range of 99% and 95% of the maximum output power density are shown. With increasing backside illumination, the optimal top-cell bandgap shifts to lower values, while sensitivity is unchanged. For luminescent coupling, the optimal bandgap remains unchanged but the 99%- and 95% bands broaden towards lower bandgaps.

3.2. Estimating reasonable values of luminescent-coupling efficiency

Now, as we have studied how luminescent coupling can improve the performance of bottom-cell limited tandem solar cells [see Figs. 3(b,d)], we investigate, which lumines-

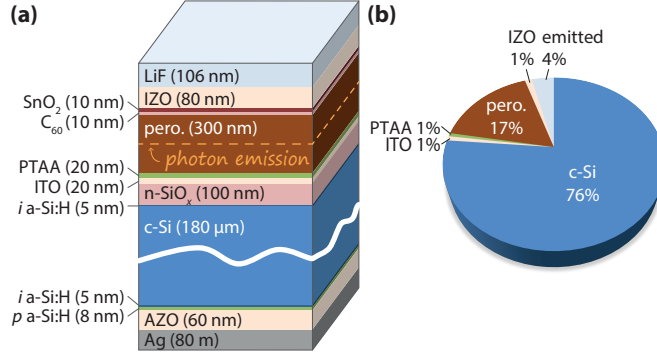


Figure 4: (a) The tandem solar cell structure used for estimating the fraction of photons, which are generated in the perovskite layer and reach the silicon wafer. The structure is based on recent high-end perovskite/silicon tandem solar cells.^{39,40} The dotted line indicates the middle of the perovskite layer (150 nm depths). In our calculations, we assumed the light emission from this depth. (b) Relative distribution of photons with 795 nm wavelength, which are isotropically emitted in the center of the perovskite layer. While around 76% are absorbed by the silicon wafer, around 17% are reabsorbed by the emitting perovskite layer. Only $\approx 4\%$ leave the solar cell structure.

cent coupling efficiencies are realistic in perovskite/silicon tandem solar cells from an optical point of view.

Increasing the power conversion efficiency of solar cells towards the theoretical limit can be realized by improving the external luminescence quantum efficiency (ELQE) of the cell in open circuit (OC), or in the other words — by suppressing non-radiative recombination.^{31,32} Despite the direct bandgap of metal halide perovskite semiconductors, initially reported ELQE values for perovskite solar cells were extremely low ($\approx 10^{-4}\%$).³³ Then, tremendous growth was demonstrated for perovskite solar cells reaching an ELQE of 0.5%,³⁴ which is equal to the record for silicon cells.³⁵ Recently, Liu and co-workers realized a single junction perovskite solar cell with 8.4% ELQE.⁸ Note that record ELQE values of the champion GaAs cells do not exceed 25%,^{36,37} even though internal luminescence quantum efficiency (ILQE) values of 99.7% have experimentally been shown for GaAs devices.³⁸

As a first step to estimate the luminescent coupling efficiency for a cell with the experimentally measured 8.4% ELQE, we calculate the fraction E_t^{int} of light generated in the perovskite layer, which leaves the solar cell structure, using the optical simulation tool GenPro4. We assume a perovskite thickness of 400 nm and an emission wavelength of 795 nm, which corresponds to the bandgap of the perovskite methylammonium lead

iodide (MAPbI₃) of 1.56 eV, in accordance with the device architecture used by Liu *et al.*⁸ As shown in appendix D, we revealed $E_t^{\text{int}} = 7.8\%$ for this configuration, which is independent of the emission depths in the perovskite layer. The rest of the generated light cannot leave the solar cell structure, because it either radiates in directions outside the emission cone, which has an opening angle of 23.8° for MAPbI₃ at 795 nm,⁴¹ or it is absorbed before it can leave the solar cell. The experimental ELQE (8.4%) being larger than the numerical value $E_t^{\text{int}} = 7.8\%$ shows that a high ILQE was achieved. For semiconductors with high ILQE, photon recycling,⁴² i.e. the re-absorption of previously emitted photons within the perovskite, can increase the ELQE to values higher than what would be expected from the optical simulations without photon recycling.⁴³

With a simulation, where we assumed that light emitted in the perovskite layer can either escape the cell, is parasitically absorbed in different layers or is reabsorbed in the perovskite (and then re-emitted with the probability of the ILQE) we estimate the ILQE of the best cell from Liu *et al.*⁸ to be around 65%. This is in line with simulations from Cho *et al.* on perovskite-based light emitting diodes, where they calculate that an ILQE of 60% is sufficient to reach an ELQE equal to the purely optical expectation if photon recycling is considered.⁴³

Figure 4(a) shows the perovskite/silicon tandem solar cell structure, which we used to study coupling of emitted light by the perovskite layer into silicon. This structure is based on recent high-end tandem solar cells,^{39,40} but in contrast to them we used MAPbI₃ as perovskite material in order to be consistent with the single-junction results discussed above. For an emission wavelength of 795 nm, 76% of the light generated in perovskite reaches the silicon layer. This value is almost independent from the emission depths in the perovskite layer, as shown in appendix D. Only 4% of the generated light leave the solar cell structure into air and 17% are reabsorbed in the perovskite layer, which can contribute to photon recycling. More details of the optical tandem-cell simulations are shown in Fig. 8 in appendix D.

Finally, with the perovskite layer having ILQE $\approx 65\%$, we can expect to have overall luminescent-coupling efficiencies around $\eta_{\text{LC}}^{\text{max}} \approx 56\%$, where we used eqn (26) from appendix D. However, it should be noted that Liu *et al.* measured the ELQE with an illumination of one sun without charge-carrier extraction (open circuit condition, in which all photo-generated carriers should recombine). When charge carriers are extracted in solar cell operation the ratio of radiative to non-radiative recombination might change considerably.⁴⁴ Further research is needed to assess realistic radiative efficiencies at low recombination currents. In any case, we provide a positive answer on the fundamental question: a significant fraction of light emitted by the perovskite sub-cell can reach the silicon wafer. This can change a paradigm in developing optimal perovskite materials for efficient tandem solar cells.

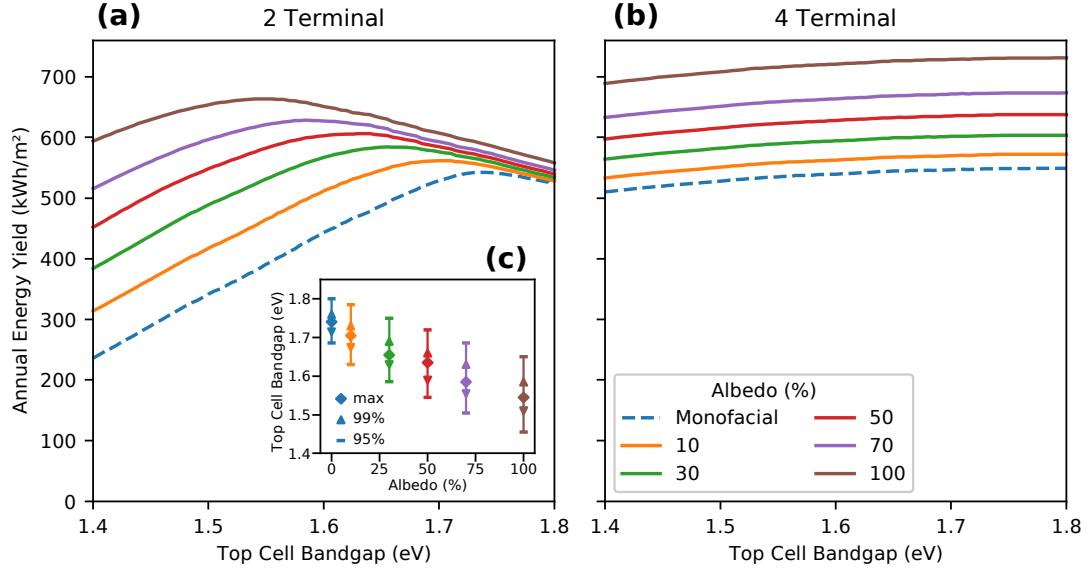


Figure 5: Energy yield for bifacial and monofacial tandem power plants simulated for Seattle with (a) two-terminal and (b) four-terminal cells connection for different albedo values. The inset (c) shows the optimal top-cell bandgap for different levels of albedo. The diamonds mark the ideal bandgap with maximum energy yield; the arrowheads and the dash marks span the ranges where at least 99% and 95% of the maximum energy yield is achieved. All simulations were performed with a module distance $d = 8$ m and mounting height of $h = 0.5$ m. The tilt angle was optimized for every data point. Monofacial tandems are simulated with albedo $A = 0\%$

Table 1: Results from energy yield calculations of two-terminal tandem cells for different albedo scenarios using average meteorological year data for Seattle with module height $h = 0.5$ m and module distance $d = 8$ m. *"Bifacial Gain" denotes the gain in irradiance.

| Type | Albedo (%) | Bifacial Gain* (%) | Opt. Bandgap (eV) | Energy Yield (kWh/m ² /a) |
|------------|------------|--------------------|-------------------|--------------------------------------|
| Monofacial | 0 | — | 1.74 | 543 |
| | 10 | 5.5 | 1.70 | 562 |
| | 30 | 12.7 | 1.66 | 584 |
| Bifacial | 50 | 19.7 | 1.64 | 606 |
| | 70 | 27.1 | 1.59 | 628 |
| | 100 | 37.4 | 1.54 | 664 |

3.3. Energy yield under realistic weather conditions

Under realistic conditions, the illumination on a solar module in a large photovoltaic field consisting of periodic rows of solar panels will significantly differ from standard testing conditions. The spectral distribution and irradiance of light in the outdoors is constantly changing and the illumination on the backside is highly dependent on the layout of the PV field. Fig 5 shows the result of energy yield calculations for bifacial and monofacial tandem solar modules for different bandgaps and varying levels of albedo in Seattle, USA and compares the performance of two- and four-terminal solar cells. The four-terminal cells show only a small dependence on the top-cell bandgap with the optimum at the upper limit of the simulated range (1.8 eV) and a monotonic decrease towards 1.5 eV. Increasing the albedo increases the energy yield but leaves character of the bandgap dependence unchanged.

In contrast, the two-terminal cells are strongly affected by changing the top-cell bandgap. Similar to the results for STC [Fig. 3(a)], there is a well-defined maximum for the bandgap with reduced energy yield for higher or lower values. The ideal top cell bandgap for monofacial cells shifts from of 1.71 eV for STC to 1.74 eV for Seattle.

With increasing albedo, the optimal top-cell bandgap shifts to lower values. The additional light impinging onto the backside is exclusively absorbed by the bottom cell. Reducing the bandgap of the top cell will increase their photocurrent density at the cost of the bottom cell. Thus, the two subcells can be made current-matched again by reducing the top-cell bandgap.

Table 1 summarizes the results from the energy yield calculations for photovoltaic modules with two-terminal tandem cells for different albedo values. For a realistic albedo of $A = 30\%$ corresponding to grey cement⁴⁵ the optimal bandgap shows a shift

of 0.08 eV with respect to a monofacial cell. In this scenario the energy yield is increased by 7.5%, which is significantly smaller than the 12.7 % gain of irradiance.

One reason for the increase of energy yield being smaller than the increase of irradiance is that light reaching the back side can only be utilized with the single junction power conversion efficiency of the bottom cell. Further, for two-terminal tandem solar cells decreasing the top-cell bandgap to ensure current matching reduces the overall open-circuit voltage and hence the power conversion efficiency.

This could lead to the conclusion that bifaciality is less beneficial for two-terminal tandem solar cells than for single junction solar cells. However, considering the electronic material quality of state-of-the-art perovskites,¹⁴ the effect of bandgap-shift might be relevant. In principle organic/inorganic perovskites can be fabricated with continuously tunable bandgaps.^{14,46} However, not all bandgap-materials can be fabricated with the same electronic quality. Fabricating high-quality perovskite semiconductors with bandgaps in the range of 1.70-1.75 eV is still a very challenging task and previous results show higher quality semiconductors in the region of 1.60-1.65 eV.¹³

Operation of perovskite/silicon tandem solar cells in bifacial configuration allows to utilize 1.60-1.65 eV bandgap perovskites for optimal performance. This enables using current high-quality perovskite absorber layers in the tandem device.

Figure 6 shows the effect of the top cell bandgap on the annual energy yield for mono- and bifacial two-terminal tandem PV modules simulated for Seattle, USA, with various levels of luminescent coupling. With an increasing luminescent coupling efficiency the energy yield becomes more and more independent from the bandgap of the top cell. Also, the maximum energy yield increases slightly and shifts a bit towards lower bandgaps. As the spectral distribution of outdoor illumination changes with time, there will always be situations where the top or bottom cells generate different photocurrent densities. Therefore, the optimal top-cell bandgap for outdoor performance will always be a compromise, which delivers the best balance over time.⁴⁷ With increasing luminescent coupling efficiency the losses from periods, where the cell is bottom-cell limited, will become smaller while losses from top cell limitation are not affected.⁴⁸ This explains the shift of the optimal bandgap to lower values, where the overall absorption in the top cell is increased. As an example, the energy yield of perovskite/silicon tandem solar cells with 1.64 eV bandgap triple cation perovskite top cell is found to increase by 21.5% when additionally considering a luminescent coupling efficiency of 30% and bifacial operation on a 30% reflective ground.

Four-terminal tandem solar cells barely show any performance improvement because of luminescent coupling, as both subcells are operated individually at their maximum power point, where only very little radiative recombination is present.

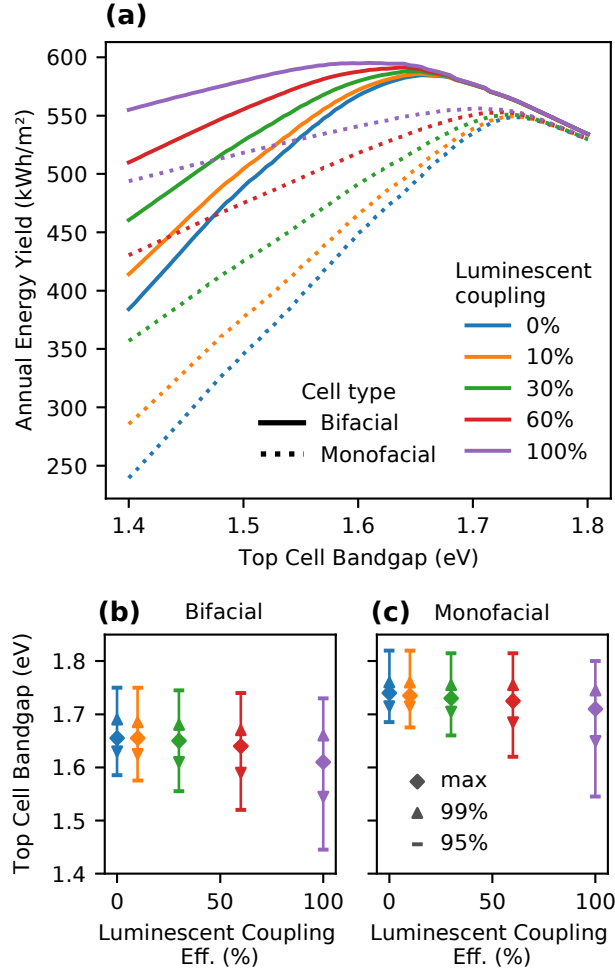


Figure 6: (a) Annual energy yield for mono- and bifacial two-terminal perovskite/silicon tandem solar cell modules simulated for Seattle with various levels of luminescent coupling. The sub figures shows the optimal top-cell bandgap for different levels of luminescent coupling of (a) bifacial and (c) monofacial tandem cells. The diamonds mark the ideal bandgap with maximum energy yield; the arrowheads and the dash marks span the ranges where at least 99% and 95% of the maximum energy yield is achieved. All simulations were performed with a module distance $d = 8$ m and $d = 0.5$ m mounting height. Bifacial operation is calculated with albedo $A = 30\%$. The module tilt angle θ_m was optimized for every data point.

4. Conclusions

In conclusion, we calculated the energy yield of perovskite/silicon tandem solar cells considering luminescent coupling between the two sub-cells and bifacial illumination of the device. To do so, we first studied idealized solar cells by using the Shockley-Queisser limit and Richter's limit for the perovskite and the silicon sub-cells, respectively. We found that additional backside illumination around 10%-20% is sufficient to shift the optimum perovskite top-cell bandgap in two-terminal tandem solar cells from 1.71 eV to the 1.60-1.64 eV range. We further found that luminescent coupling can strongly reduce the current-mismatch if the tandem solar cell is bottom-cell limited.

As a second step, we performed optical simulations in order to evaluate the relevance of luminescent coupling for perovskite/silicon tandem solar cells. On the basis of experimental photoluminescent quantum yield values we found that more than 50% of excess electron-hole pairs generated in the perovskite top cell can be re-used by the silicon bottom cell. Particularly for configurations with perovskite top cell bandgaps below the current matching optimum this significantly enhances the energy yield.

Last, we performed energy yield calculations based on typical meteorological year (TMY3) weather data of Seattle, USA, and applied an illumination model considering the spectral irradiance at the front and back sides of a solar module in a big PV field. In agreement with the calculations using standard testing conditions, we found that the operation of perovskite/silicon tandem solar cells in bifacial configuration allows to utilize 1.60-1.65 eV bandgap perovskites for optimal performance and luminescent coupling further minimizes the impact of current-mismatch in case of (silicon) bottom-cell limited devices, i.e. less photons absorbed in the silicon than in the perovskite absorber layer. The results can change a paradigm in developing the optimum perovskite material for tandem solar cells.

A. Perovskite solar cell

We assume the current density (J) – voltage (V) characteristic of the perovskite top cell to be that of a one-diode equation,

$$J_{\text{top}}(V) = J_{0,\text{top}} \left[\exp \left(\frac{eV}{kT} \right) - 1 \right] - J_{\text{ph,top}}, \quad (7)$$

with the elementary charge e , the Boltzmann constant k , the temperature T and the photon current density $J_{\text{ph,top}}$. The dark current density $J_{0,\text{top}}$ is calculated according to the Shockley-Queisser limit,²⁶ where only radiative recombination is considered in the solar cell, while non-radiative recombination processes like Shockley-Read-Hall recombination or Auger recombination are not accounted for. For calculating the radiative

recombination rate, the solar cell is considered to be in thermal equilibrium with the surrounding at $T = 300$ K and emits like a black body for photon energies higher or equal to the perovskite bandgap E_{pero} . Therefore, we find

$$J_{0,\text{top}} = 2e\pi \int_{E_{\text{pero}}}^{\infty} \frac{2}{c^2 h^3} \frac{E^2 dE}{\exp\left(\frac{E}{kT} - 1\right)}, \quad (8)$$

where the first factor 2 arises from the solar cell emitting thermal radiation from both the front and back sides. For the photon current density we assume that the perovskite absorbs step-like: all photons with energies larger or equal to the bandgap are assumed to be absorbed in the solar cell,

$$J_{\text{ph,top}} = e \int_0^{\frac{hc}{E_{\text{pero}}}} \Phi_f(\lambda) d\lambda, \quad (9)$$

where Φ_f is the photon flux impinging on the solar cell front. (For calculating the SQ limit, Φ_f would be according to the AM1.5 standardized solar spectrum.)

B. Silicon solar cell

Silicon is an indirect-bandgap material, which means that also Auger recombination has to be considered – the Shockley-Queisser limit would overestimate the theoretical limit. Here, we follow a recent approach by Richter *et al.*, who calculated the theoretical limit for silicon solar cells to be 29.4%.²

In the Richter limit, the J - V characteristic of a silicon solar cell is given by

$$J_{\text{bot}}(V) = e \cdot d_{\text{Si}} \cdot R_{\text{intr}}(V) - J_{\text{ph,bot}} \quad (10)$$

with the silicon thickness d_{Si} and the voltage-dependent intrinsic radiation rate R_{intr} , which accounts for both radiative and Auger recombination. We use a linear model for low doping concentrations according to eqn (21) of a work by Richter *et al.*⁴⁹

$$R_{\text{intr}} = np \left(8.7 \cdot 10^{-29} n_0^{0.91} + 6.0 \cdot 10^{-30} p_0^{0.94} + 3.0 \cdot 10^{-29} \Delta n^{0.92} + B_{\text{tot}} \right) \quad (11)$$

with the electron and hole concentrations n and p , the respective equilibrium concentrations n_0 and p_0 , which are connected to each other via $n = n_0 + \Delta n$ and $p = p_0 + \Delta n$ with the excess carrier concentration Δn , given by

$$\Delta n = n_i \left(\exp \frac{eV}{2kT} - 1 \right). \quad (12)$$

The effective intrinsic carrier concentration is given by

$$n_i = n_0 = n_p = n_{i,0} \exp \frac{\Delta E_{\text{Si}}}{2kT} \quad (13)$$

with $n_{i,0} = 8.28 \cdot 10^9 \text{ cm}^{-3}$ and $\Delta E_{\text{Si}} = 0.005 \text{ eV}$, which accounts for *bandgap narrowing*². Finally, the coefficient $B_{\text{tot}} = (1 - P_{\text{PR}})B_{\text{low}}$ contains the radiative recombination coefficient for low-doped Si, $B_{\text{low}} = 4.73 \cdot 10^{-15} \text{ cm}^3 \text{ s}^{-1}$,⁵⁰ and the *photon-recycling* probability P_{PR} , as described by Richter *et al.*²

The short-circuit current density for the silicon cell is given by

$$J_{\text{sc, Si}} = e \int_{\lambda_{\text{pero}}}^{\lambda_{\text{Si}}} A(\lambda) \Phi_f(\lambda) d\lambda + e \int_0^{\lambda_{\text{Si}}} A(\lambda) \Phi_b(\lambda) d\lambda + J_{\text{LC}} \quad (14)$$

with the photon fluxes Φ_f and Φ_b reaching the front and back sides of the silicon cell, respectively, and the current density J_{LC} due to *luminescent coupling*, which is treated in appendix C below. The absorption $A(\lambda)$ is calculated according to the Tiedje-Yablonovitch limit,⁵¹ hence we assume perfect light trapping.

$$A(\lambda) = \frac{\alpha_{\text{Si}}(\lambda)}{\alpha_{\text{Si}}(\lambda) + (4n_{\text{Si}}^2 d_{\text{Si}})^{-1}}. \quad (15)$$

Here, α_{Si} and n_{Si} are the absorption coefficient and refractive index of silicon, respectively. Assuming a sharp absorption edge as for the perovskite top cell would not be a good assumption for silicon because of its indirect bandgap characteristic, which makes silicon weakly absorbing for a large wavelength range.

C. Luminescent coupling

Luminescent coupling can affect the performance of high quality multi-junction solar cells significantly. In general, luminescent coupling describes a process, where photons generated by radiative recombination in a high-bandgap subcell are absorbed in an adjacent subcell with a lower bandgap. Different methods were developed to model luminescent coupling, most are based on equivalent circuits for diodes.⁴⁴

Here, we derive a simple model for luminescent coupling in a tandem solar cell with idealized top and bottom cells. As mentioned above, the top cell is described by a one-diode equation with infinite parallel and zero series resistance,

$$J_{\text{top}} = J_{\text{ph,top}} - J_0 \left[\exp \left(\frac{qV}{k_b T} \right) - 1 \right] = J_{\text{ph,top}} - J_{\text{rec,top}}, \quad (16)$$

where $J_{\text{ph,top}}$ is the photocurrent density from external recombination, J_0 is the saturation current density, V is the bias voltage of the top junction and $J_{\text{rec,top}}$ is the recombination current density. The recombination of the idealized top cell is exclusively radiative. Therefore, the additional current density in the bottom cell because of luminescent coupling J_{LC} can be described as

$$J_{\text{LC}} = \eta_{\text{LC}} J_{\text{rec,top}}, \quad (17)$$

where η_{LC} is the luminescent-coupling efficiency. In an idealized solar cell this efficiency only depends on the optical properties of the solar cell, because light generated in the top cell only can escape the perovskite layer through the top, where it is lost; into the bottom cell, where it can be absorbed; or it is absorbed in another layer of the solar cell, as discussed in appendix D and also shown in Fig. 4. In real solar cells, depending on the type of semiconductor and the material quality, η_{LC} is often dominated by electrical effects, because usually only a fraction of the recombination occurs radiatively.^{52,53}

The overall electrical current density in the bottom cell including LC is given by

$$J_{\text{bot}}(V_{\text{bot}}) = J_{\text{ph,bot}} - J_{\text{rec,bot}}(V_{\text{bot}}) + \eta_{LC} J_{\text{rec,top}}(V_{\text{top}}) \quad (18)$$

If the tandem cell is build as a monolithic two-terminal cell, the electrical current densities flowing through the top and bottom cells are identical,

$$J_{\text{bot}} \equiv J_{\text{top}} \equiv J_{\text{tandem}} \quad (19)$$

In order to model the J - V characteristic of a two-terminal cell with luminescent coupling, both eqn (16) and (18) need to be satisfied at the same time. To find a solution for the cell voltage, the J - V characteristic needs to be calculated as a function of the current density J_{tandem} . Therefore, the voltage-dependent recombination current density needs to be inverted. While this is easily done for a one-diode model with a cell obeying the Shockley-Queisser limit, it is not straight forwards for the characteristic of a silicon solar cell according to considerations of Richter *et al.*² We use a numerical approach by solving the forward function in the dark for a very fine grid of voltages and use a linear interpolation to approximate the inverse function. With the inverse function approximation we can calculate the power of the cell,

$$\begin{aligned} J_{\text{rec,top}} &= J_{\text{ph,top}} - J_{\text{tandem}}, \\ J_{\text{rec,bot}} &= J_{\text{ph,bot}} + \eta_{LC} \cdot J_{\text{rec,top}} - J_{\text{tandem}}, \\ P_{\text{tandem}} &= J_{\text{tandem}} \cdot [V_{\text{top}}(J_{\text{rec,top}}) + V_{\text{bot}}(J_{\text{rec,bot}}, J_{\text{rec,top}})]. \end{aligned} \quad (20)$$

Because all components of eqn (20) only depend on the current density of the tandem cell and the photocurrent densities generated in the top and bottom cells, the power can be computed very fast on a regular grid. For every time step of radiation data in the TMY3 time series we first calculate the photocurrent densities in the top and bottom cells, $J_{\text{ph,top}}$ and $J_{\text{ph,bot}}$. Subsequently we calculate the cell voltages of the subcells for a grid between 0.1 and 50 mA/cm² with a resolution of 0.1 mA/cm². With the sum of the voltages and the corresponding current density, the output power density is found, where the maximum is taken as *maximum power point* (MPP) power output.

For the case of four-terminal cells the output power density is calculated independently for each subcell. To account for luminescent coupling first the maximum power output of the top cell is evaluated. The recombination current at this working point $J_{\text{rec,top}}^{\text{mpp}}$ is then used to calculate the current contribution in the bottom cell from luminescent coupling. This contribution is in general very low, because the radiative recombination at the maximum power point is low.

$$\begin{aligned} P_{\text{top}} &= J_{\text{top}} \cdot V_{\text{top}}(J_{\text{rec,top}}), \\ P_{\text{bot}} &= J_{\text{bot}} \cdot V_{\text{bot}}(J_{\text{rec,bot}}, J_{\text{rec,top}}^{\text{mpp}}) \\ P_{\text{tandem}} &= P_{\text{top}} + P_{\text{bot}}. \end{aligned} \quad (21)$$

D. Optical modeling of luminescent coupling

We performed optical simulations to assess, (1) how much of the light generated in the perovskite layer can leave a single-junction perovskite cell, and (2) how much light reaches the silicon layer in a perovskite/silicon tandem solar cell. The optical simulations are performed with the MATLAB-based package GenPro4, which is based on the net-radiation method.²⁸ This package mimics the coherence properties of light by allowing the user to decide, in which layers light behaves coherently and incoherently, respectively.

Figure 7 illustrates the optical simulations for single-junction perovskite solar cells, based on the solar-cell structure by Liu *et al.*⁸ The layer stack, shown in Fig. 7(a), consists of Corning Eagle XG glass,⁵⁴ indium tin oxide (ITO), poly[bis(4-phenyl)(2,4,6-trimethylphenyl)amine (PTAA), methylammonium lead iodide (MAPbI₃) as perovskite,⁴¹ phenyl-C₆₁-butyric acid methyl ester (PCBM), bathocuproine (BCP),⁵⁵ and silver.⁵⁶ For ITO, PTAA and PCBM, we used in-house measured n, k data. The glass substrate was treated incoherently, all other layers were treated incoherently by GenPro4. Figure 7(b) shows the absorption of this structure, when light is incident via the glass side.

To calculate luminescence in the solar cell, we have to combine two sets of simulations. Figure 7(c) shows the simulation setup, where we study, how light emitted into the upper hemisphere interacts with the layer stack on the front side of the solar cell. To simulate emission within the perovskite layer, we assume an infinitely thick perovskite layer on bottom, from which light is incident on the structure, because GenPro4 cannot treat light emitted from within the structure. From this simulation, we can derive the fraction $E(\theta)$ of light, that leaves the solar cell when light has an angle of incidence θ in the perovskite layer. Further, the simulation delivers the reflection of the front layers $R_f(\theta)$ and the absorption $A(\theta)$ for all layers. Note that the simulation accounts for absorption in the perovskite above the position of emission. Figure 7(d) shows the sim-

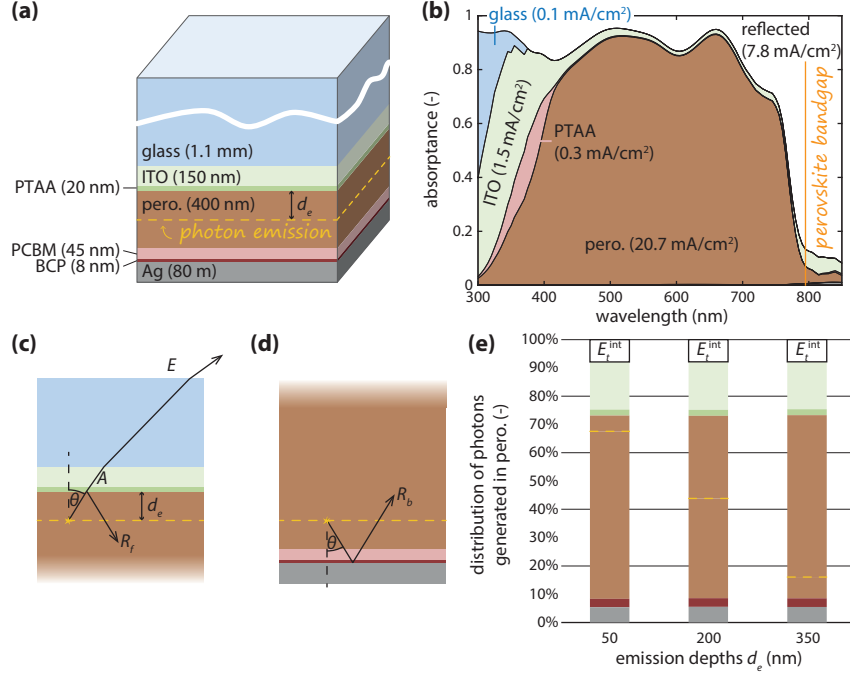


Figure 7: Optical simulations on single-junction perovskite solar cells. (a) Illustrating the solar cell layer stack, which is based on recent work by Liu *et al.*⁸ (b) Absorption profile for this layer stack when light is incident from the air above the glass. The position of the perovskite bandgap (MAPbI₃, 1.56 eV) is indicated. (c) Layer stack for assessing, how light emitted in the perovskite layer interacts with the layers above perovskite. The dashed yellow line marks the position of the light emission. (d) Same as (c), but for layers below the perovskite layer. (e) Relative distribution of photons with 795 nm wavelength, which are isotropically emitted at three different positions in the perovskite layer. The emission depths has only little effect on the fraction of light reaching the silicon. The colors correspond to the legend in (a). The yellow dashed lines separate the fraction absorbed in the perovskite above and below the position of emission.

ulation setup for the lower layers of the solar cell for light that is emitted into the lower hemisphere. To mimic the emission within the perovskite, light is simulated as incident via an infinitely thick perovskite layer on top. From this simulation, we retrieve the reflection from the back $R_b(\theta)$ and – if wanted the absorption in the different layers.

To calculate the total amount of escaping light $E_t(\theta)$, we also must take reflection from the back side into account, leading to a geometric series,

$$E_t = E (1 + R_b) \left[1 + R_f R_b + (R_f R_b)^2 + \dots \right] = \frac{E (1 + R_b)}{1 - R_f R_b}, \quad (22a)$$

where we omitted the dependency on θ for brevity. The summand R_b in the numerator accounts for light, which is emitted into the lower hemisphere and reflected back. Note that we can use eqn (22a) also for calculating the total absorption in the layers above the position of emission via replacing E with the respective absorptance A . For calculating the total absorption in layers below the position of emission, we have to slightly adapt eqn (22a) and find

$$A_t = \frac{A (1 + R_f)}{1 - R_f R_b}. \quad (22b)$$

Note that we omit effects due to coherence in eqn (22). Finally, we have to integrate over all angles, because light will be emitted isotropically in the perovskite layer.

$$E_t^{\text{int}} = \frac{1}{4\pi} \int_0^{2\pi} \int_0^{\frac{\pi}{2}} E_t \sin \theta \, d\theta \, d\phi. \quad (23)$$

By replacing E_t with the total absorptance A_t for a specific layer, the integrated absorption in that layer can be calculated. Note that the integral only extends over hemisphere, and not over the full sphere, because the other sphere is accounted for in the summands R_b and R_f in the nominators of eqn (22).

Figure 7(e) shows, where light emitted in the perovskite layer ends up for three different depths of emission d_e . We see that d_e hardly affects the picture. For all depths, the emitted fraction is $E_t^{\text{int}} = 7.8\%$. Around 65% are reabsorbed in the perovskite layer. The largest parasitic absorption occurs in the ITO, where around 17% are lost. If no light was reflected from the back ($R_b = 0$) around 3.6% of the emitted light would leave the layer stack. This fraction is less than half of E_t^{int} , because light, which is originally emitted into the upper hemisphere but then reflected back into the lower hemisphere, can be reflected upwards again when the back is reflected but it is lost otherwise. The low fraction of emission can be explained by total internal reflection. At 795 nm wavelength, for which we study luminescence, the refractive index of the perovskite is $n = 2.47$.⁴¹ Hence, all light that is emitted into angles larger than $\theta > 23.83^\circ$ is trapped inside they layer stack because of total internal reflection. Note, that we did not consider photon

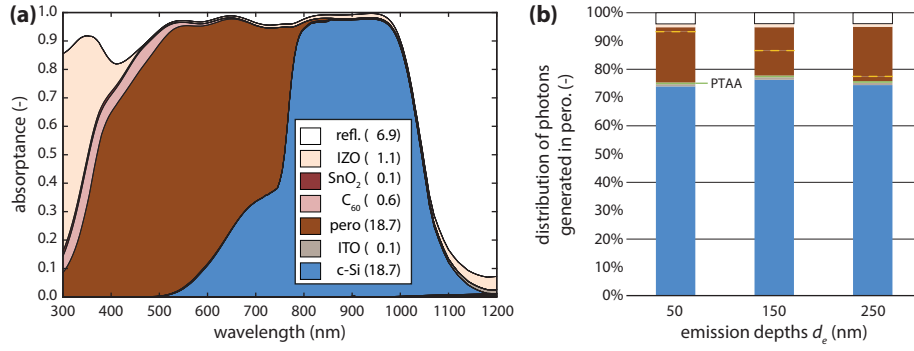


Figure 8: More details on the optical simulations on the tandem solar cell structure, which is discussed in Fig. 4. (a) The absorption profile for the tandem solar cell structure shown in Fig. 4(a), when light is incident from top. The numbers in brackets indicate the photocurrent density equivalent to the absorption in the layer in mA/cm². (b) Relative distribution of photons with 795 nm wavelength, which are isotropically emitted at three different positions in the perovskite layer. The emission depths has only little effect on the fraction of light reaching the silicon. The colors correspond to the legend in (a) except PTAA, which is not visible in (a). The yellow dashed lines separate the fraction absorbed in the perovskite above and below the position of emission.

recycling here: light, that is reabsorbed in the perovskite can lead to another generated photon.

The layer stack considered for the simulations of the tandem solar cell is shown in Fig. 4(a): lithium fluoride (LiF),⁵⁷ indium zinc oxide (IZO), silicon oxide (SnO₂), C₆₀, MAPbI₃,⁴¹ PTAA, ITO, intrinsic amorphous hydrogenated silicon (*i* a-Si:H), crystalline silicon (c-Si),⁵⁸ *i* a-Si:H, *p*-doped a-Si:H, aluminium-doped zinc oxide (AZO), and silver (Ag).⁵⁶ For all materials, where no reference is given, the *nk*-data were determined in-house.

Figure 8 shows more details on the optical simulations on the tandem solar cell structure, which is discussed in Fig. 4 of the main manuscript. Figure 8(a) shows the absorption profile for the tandem solar cell structure shown in Fig. 4(a), when light is incident from top. The layer thicknesses were adapted such, that we have current matching between top and bottom cells for front-side illumination under STC. Figure 8(b) shows, how the emission depth of the light in the perovskite layer affects the fractions of the emitted light ending up in the different layers. As for the single-junction cells [Fig. 7(e)], the emission depths has only little effect.

Photon recycling should be considered when estimating the ILQE from the ELQE. We use a simple model for a cell in open circuit condition where the charge carriers created by the external light source can undergo a chain of emission and reabsorption events. In a first step the charge carriers can be either recombine radiatively with probability ILQE or non-radiatively with probability (1 – ILQE). In the next step the emitted photons can either leave the cell with probability E_t^{int} , be absorbed parasitically in non-active areas with probability A_{para} or reabsorbed in the perovskite with probability $A_{\text{pero}} = 1 - E_t^{\text{int}} - A_{\text{para}}$. A_{pero} , E_t^{int} and A_{para} can be extracted from the optical simulations described above. The reabsorbed light can undergo the same processes as the direct absorbed light from the external source. This chain of events can be represented as a geometric series to calculate the ELQE,

$$\begin{aligned} \text{ELQE} &= E_t^{\text{int}} \cdot \text{ILQE} \left[1 + A_{\text{pero}} \cdot \text{ILQE} + (A_{\text{pero}} \cdot \text{ILQE})^2 + \dots \right] \\ &= \frac{E_t^{\text{int}} \cdot \text{ILQE}}{1 - A_{\text{pero}} \cdot \text{ILQE}}. \end{aligned} \quad (24)$$

This function can be inverted to solve for ILQE,

$$\text{ILQE} = \left(\frac{E_t^{\text{int}}}{\text{ELQE}} + A_{\text{pero}} \right)^{-1}. \quad (25)$$

We can estimate an upper bound for the luminescence coupling efficiency $\eta_{\text{LC}}^{\text{max}}$ by replacing E_t^{int} with A_{Si} in eqn (24),

$$\eta_{\text{LC}}^{\text{max}} = \frac{A_{\text{Si}} \cdot \text{ILQE}}{1 - A_{\text{pero}} \cdot \text{ILQE}}. \quad (26)$$

For estimating $\eta_{\text{LC}}^{\text{max}}$ we use the values for 150 nm emission depths, shown in Fig. 8(b): $A_{\text{Si}} = 0.763$ and $A_{\text{pero}} = 0.171$. Assuming $\text{ILQE} = 65\%$, just as for the single-junction cell discussed above, we find $\eta_{\text{LC}}^{\text{max}} \approx 56\%$.

Conflicts of interest

There are no conflicts to declare.

Acknowledgements

P. T. thanks the Helmholtz Einstein International Berlin Research School in Data Science (HEIBRiDS) for funding. We acknowledge the German Federal Ministry for Education and Research (BMBF) for support from the SNaPSHoTs project in the framework of the German-Israeli bilateral R&D cooperation in the field of applied nanotechnology (grant no. 01IO1806). The results were obtained at the Berlin Joint Lab for Optical Simulations for Energy Research (BerOSE) and the Helmholtz Excellence Cluster SOLARMATH of Helmholtz-Zentrum Berlin für Materialien und Energie, Zuse Institute Berlin and Freie Universität Berlin.

References

- [1] ITRPV, *11th Edition of the International Technology Roadmap Photovoltaics*, Vdma technical report, 2020.
- [2] A. Richter, M. Hermle and S. W. Glunz, *IEEE Journal of Photovoltaics*, 2013, **3**, 1184–1191.
- [3] R. Kopecek and J. Libal, *Nature Energy*, 2018, **3**, 443–446.
- [4] T. S. Liang, M. Praveetoni, C. Deline, J. S. Stein, R. Kopecek, J. P. Singh, W. Luo, Y. Wang, A. G. Aberle and Y. S. Khoo, *Energy Environ. Sci.*, 2019, **12**, 116–148.
- [5] N. Ishikawa and S. Nishiyama, Presented at the 3rd Bifi PV Workshop, Miyazaki, Japan, 2016.
- [6] K. Jäger, P. Tillmann and C. Becker, *Optics Express*, 2020, **28**, 4751.
- [7] J. Werner, B. Niesen and C. Ballif, *Advanced Materials Interfaces*, 2018, **5**, 1700731.

- [8] Z. Liu, L. Krückemeier, B. Krogmeier, B. Klingebiel, J. A. Márquez, S. Levchenko, S. Öz, S. Mathur, U. Rau, T. Unold and T. Kirchartz, *ACS Energy Letters*, 2019, **4**, 110–117.
- [9] National Renewable Energy Laboratory, *Best Research-Cell Efficiency Chart*, Nrel technical report, 2020.
- [10] B. Chen, S.-W. Baek, Y. Hou, E. Aydin, M. D. Bastiani, B. Scheffel, A. Proppe, Z. Huang, M. Wei, Y.-K. Wang, E.-H. Jung, T. G. Allen, E. V. Kerschaver, F. P. G. de Arquer, M. I. Saidaminov, S. Hoogland, S. D. Wolf and E. H. Sargent, *Nat. Comm.*, 2020, **11**, 1257.
- [11] T. Leijtens, K. A. Bush, R. Prasanna and M. D. McGehee, *Nature Energy*, 2018, **3**, 828–838.
- [12] IEC:60904-3: *Photovoltaic devices - Part 3: Measurement principles for terrestrial photovoltaic (PV) solar devices with reference spectral irradiance data*, 2008.
- [13] M. Jošt, L. Kegelmann, L. Korte and S. Albrecht, *Advanced Energy Materials*, 2020, 1904102.
- [14] E. L. Unger, L. Kegelmann, K. Suchan, D. Sörell, L. Korte and S. Albrecht, *J. Mater. Chem.A*, 2017, **5**, 11401–11409.
- [15] R. Schmager, M. Langenhorst, J. Lehr, U. Lemmer, B. S. Richards and U. W. Paetzold, *Optics Express*, 2019, **27**, A507–A523.
- [16] A. Onno, N. Rodkey, A. Asgharzadeh, S. Manzoor, Z. J. Yu, F. Toor and Z. C. Holman, *Joule*, 2020, **4**, 580–596.
- [17] H. Imran, I. Durrani, M. Kamran, T. M. Abdolkader, M. Faryad and N. Z. Butt, *IEEE Journal of Photovoltaics*, 2018, **8**, 1222–1229.
- [18] O. Dupré, A. Tuomiranta, Q. Jeangros, M. Boccard, P.-J. Alet and C. Ballif, *IEEE Journal of Photovoltaics*, 2020, **10**, 714–721.
- [19] R. Asadpour, R. V. K. Chavali, M. Ryyan Khan and M. A. Alam, *Applied Physics Letters*, 2015, **106**, 243902.
- [20] M. Ryyan Khan and M. A. Alam, *Applied Physics Letters*, 2015, **107**, 223502.
- [21] A. Brown and M. Green, Conference Record of the Twenty-Ninth IEEE Photovoltaic Specialists Conference, 2002., 2002, pp. 868–871.

- [22] M. A. Steiner and J. F. Geisz, *Applied Physics Letters*, 2012, **100**, 251106.
- [23] M. Z. Shvarts, M. A. Mintairov, V. M. Emelyanov, V. V. Evstropov, V. M. Lantratov and N. K. Timoshina, *AIP Conference Proceedings*, 2013, **1556**, 147.
- [24] N. L. A. Chan, T. Thomas, M. Führer and N. J. Ekins-Daukes, *IEEE Journal of Photovoltaics*, 2014, **4**, 1306–1313.
- [25] D. J. Friedman, J. F. Geisz and M. A. Steiner, *IEEE Journal of Photovoltaics*, 2014, **4**, 986–990.
- [26] W. Shockley and H. J. Queisser, *Journal of Applied Physics*, 1961, **32**, 510–519.
- [27] Z. Wang, Q. Lin, B. Wenger, M. G. Christoforo, Y.-H. Lin, M. T. Klug, M. B. Johnston, L. M. Herz and H. J. Snaith, *Nature Energy*, 2018, **3**, 855–861.
- [28] R. Santbergen, T. Meguro, T. Suezaki, G. Koizumi, K. Yamamoto and M. Zeman, *IEEE J. Photovolt.*, 2017, **7**, 919–926.
- [29] P. Tillmann, K. Jäger and C. Becker, *Sustainable Energy & Fuels*, 2020, **4**, 254–264.
- [30] S. Wilcox and W. Marion, *Users manual for TMY3 data sets*, National Renewable Energy Laboratory Technical Report NREL/TP-581-43156, National Renewable Energy Laboratory Golden, CO, 2008.
- [31] U. Rau, *Physical Review B - Condensed Matter and Materials Physics*, 2007, **76**, 085303.
- [32] O. D. Miller, E. Yablonovitch and S. R. Kurtz, *IEEE Journal of Photovoltaics*, 2012, **2**, 303–311.
- [33] K. Tvingstedt, O. Malinkiewicz, A. Baumann, C. Deibel, H. J. Snaith, V. Dyakonov and H. J. Bolink, *Scientific Reports*, 2014, **4**, 1–7.
- [34] D. Bi, W. Tress, M. I. Dar, P. Gao, J. Luo, C. Renevier, K. Schenk, A. Abate, F. Giordano, J. P. Correa Baena, J. D. Decoppet, S. M. Zakeeruddin, M. K. Nazeeruddin, M. Grätzel and A. Hagfeldt, *Science Advances*, 2016, **2**, e1501170.
- [35] M. A. Green, *Progress in Photovoltaics: Research and Applications*, 2012, **20**, 472–476.
- [36] B. M. Kayes, H. Nie, R. Twist, S. G. Spruytte, F. Reinhardt, I. C. Kizilyalli and G. S. Hignashi, *Conference Record of the IEEE Photovoltaic Specialists Conference*, 2011, pp. 000004–000008.
- [37] A. Braun, E. A. Katz, D. Feuermann, B. M. Kayes and J. M. Gordon, *Energy and Environmental Science*, 2013, **6**, 1499–1503.

- [38] I. Schnitzer, E. Yablonovitch, C. Caneau and T. J. Gmitter, *Applied Physics Letters*, 1993, **62**, 131–133.
- [39] M. Jošt, E. Köhnen, A. B. Morales-Vilches, B. Lipovšek, K. Jäger, B. Macco, A. Al-Ashouri, J. Krč, L. Korte, B. Rech, R. Schlatmann, M. Topič, B. Stannowski and S. Albrecht, *Energy Environ. Sci.*, 2018, **11**, 3511–3523.
- [40] E. Köhnen, M. Jošt, A. B. Morales-Vilches, P. Tockhorn, A. Al-Ashouri, B. Macco, L. Kegelmann, L. Korte, B. Rech, R. Schlatmann, B. Stannowski and S. Albrecht, *Sustainable Energy & Fuels*, 2019, **3**, 1995–2005.
- [41] J. A. Guerra, A. Tejada, L. Korte, L. Kegelmann, J. A. Töfflinger, S. Albrecht, B. Rech and R. Weingärtner, *J. Appl. Phys.*, 2017, **121**, 173104.
- [42] R. Brenes, M. Laitz, J. Jean, D. W. Dequillettes and V. Bulović, *Physical Review Applied*, 2019, **12**, 014017.
- [43] C. Cho, B. Zhao, G. D. Tainter, J. Y. Lee, R. H. Friend, D. Di, F. Deschler and N. C. Greenham, *Nature Communications*, 2020, **11**, 611.
- [44] J. Jia, Y. Miao, Y. Kang, Y. Huo, M. Mazouchi, Y. Chen, L. Zhao, H. Deng, P. Supaniratisai, S. H. AlQahtani and J. S. Harris, *Optics Express*, 2015, **23**, A219.
- [45] R. Levinson and H. Akbari, *Cement and Concrete Research*, 2002, **32**, 1679 – 1698.
- [46] G. E. Eperon, S. D. Stranks, C. Menelaou, M. B. Johnston, L. M. Herz and H. J. Snaith, *Energy and Environmental Science*, 2014, **7**, 982–988.
- [47] M. T. Hörantner and H. J. Snaith, *Energy & Environmental Science*, 2017, **10**, 1983–1993.
- [48] Y. Okada, N. Ahsan, R. Tamaki, K. Yoshida and B. Yu Jeco, *33rd European Photovoltaic Solar Energy Conference and Exhibition*, 2017, 1236–1240.
- [49] A. Richter, S. W. Glunz, F. Werner, J. Schmidt and A. Cuevas, *Phys. Rev. B*, 2012, **86**, 165202.
- [50] T. Trupke, M. A. Green, P. Würfel, P. P. Altermatt, A. Wang, J. Zhao and R. Corkish, *Journal of Applied Physics*, 2003, **94**, 4930.
- [51] T. Tiedje, E. Yablonovitch, G. D. Cody and B. G. Brooks, *IEEE Transactions on Electron Devices*, 1984, **31**, 711–716.
- [52] T. Sogabe, A. Ogura, C. Y. Hung, V. Evstropov, M. Mintairov, M. Shvarts and Y. Okada, *Applied Physics Letters*, 2013, **103**, 263907.

- [53] S. H. Lim, J.-J. Li, E. H. Steenbergen and Y.-H. Zhang, *Progress in Photovoltaics: Research and Applications*, 2013, **21**, 344–350.
- [54] C. V. Cushman, B. A. Sturgell, A. C. Martin, B. M. Lunt, N. J. Smith and M. R. Linford, *Surface Science Spectra*, 2016, **23**, 55–60.
- [55] Z. Liu, C. Kwong, C. Cheung, A. Djurišić, Y. Chan and P. Chui, *Synthetic Metals*, 2005, **150**, 159–163.
- [56] P. B. Johnson and R. W. Christy, *Physical Review B*, 1972, **6**, 4370–4379.
- [57] H. H. Li, *J. Phys. Chem. Ref. Data*, 1976, **5**, 329–528.
- [58] M. A. Green and M. J. Keevers, *Progress in Photovoltaics: Research and Applications*, 1995, **3**, 189–192.